Original Article

Processing, microstructural, and mechanical characterization of extruded 6013 aluminum alloy

Renata Querolaine Torres [1]
Gisele Fabiane Costa Almeida [2]*
Carolina Sayuri Hattori [3]
Luiz Carlos da Silva Filho [1]

Abstract

The 6013-aluminum alloy is used in automotive applications due to its higher levels of mechanical strength. This work aimed to characterize the microstructural and mechanical properties of this alloy obtained in various stages of industrial processing. The alloy was subjected to homogenization, extrusion and solubilization, tempering, and artificial aging processes. The microstructure was characterized by optical (OM), scanning electron (SEM), transmission electron microscopy (TEM), and X-ray diffraction technique (XRD). In the as-cast condition, the present phases in the 6013-alloy were almost completely precipitated at the α phase grain boundaries. Homogenization and solubilization during the extrusion process strongly reduced the amount of these precipitates. The α-phase morphology showed a heterogeneous distribution along the thickness of the extruded profile, with recrystallized grains close to the surface and many work-hardened grains inside. The aging heat treatment significantly increased the extruded profile mechanical strength. In the analysis of the present phases, it was possible to identify, in addition to the α-Al phase, the compounds precipitated in greater quantity, such as Mg_2Si, β-AlFeSi, and α-AlFeSi.

Keywords: High strength aluminum alloys; Al-Mg-Si-Cu Alloys; Microstructural characterization.

1 Introduction

The transport industry is increasingly focused on performance, efficiency, and reducing fuel consumption and greenhouse gas emissions. To achieve these goals, a continual search for materials to make vehicles lighter and enhance component efficiency has been performed [1]. Aluminum alloys are gaining attraction due to their lower density compared to steel, promising efficiency improvements. High-strength aluminum alloys can maintain vehicle safety while significantly reducing mass [2]. The 6XXX series alloys, with silicon and magnesium as primary alloying elements, have been extensively researched for their strength properties, offering potential for automotive applications. Alloy modifications aim to meet specific automotive requirements [3]. Research on the precipitates effect on ductility and fracture behavior in these alloys suggests that extrusion processes can mitigate ductility issues caused by precipitates [4-6]. While some alloys in the 6000 series exhibit reduced ductility with increasing yield stress, the 6061-alloy stands out for its combination of high strength and ductility, attributed to smaller precipitate size. The 6013-aluminum alloy, with more alloying elements, shows promise for automotive use due to its higher mechanical strength levels [7]. Studies on the precipitation kinetics in aluminum alloys have primarily focused on common 6XXX series alloys, but there's potential for broader application, including the 6013-alloy. Bakare [8] mentions that the extrusion process involves numerous conditions that impact profile productivity, such as the complex thermomechanical cycle, chemical reactions between hot aluminum and tool steel equipment, and various process parameters. A better understanding of the interaction between billet preheating times and temperature, extrusion exit speed, and aging kinetics can lead to improvements in this process. Odoh [9] performed one research to help understand the extrudability of some Al-Mg-Si alloys as well as the effect of extrusion conditions on final mechanical properties, performing both laboratory scale and industrial extrusion trials as well as mechanical and microstructural characterization of the extruded materials. Bai at al characterized the microstructural and mechanical properties of the 6013-alloy throughout its industrial processing stages, from casting to aging, correlating microstructure with mechanical properties [10].

The main objective of this work is to investigate the microstructural evolution and tensile mechanical properties of 6013 aluminum alloy at different stages of industrial processing, including solidification, homogenization,

[1]*Faculdade de Ciências, Universidade Estadual Paulista – UNESP, Bauru, SP, Brasil.*
[2]*Universidade Presbiteriana Mackenzie, São Paulo, SP, Brasil.*
[3]*Centro de Ciências e Tecnologia dos Materiais, Instituto de Pesquisas Energéticas e Nucleares - IPEN, São Paulo, Brasil.*

**Corresponding author: gisele_fab@hotmail.com*
Adresses: renata_querolaine@hotmail.com; luiz.carlos@unesp.br;carolina.hattori@cba.com.br

extrusion, solution aging, and thermal aging. The study aims to understand how each processing stage affects the distribution and volume fraction of precipitated phases, as well as the relationship between microstructural changes and the mechanical performance of the material, particularly in terms of tensile strength.

2 Materials and methods

The 6013-alloy billets produced from Direct Chill (DC) casting were used for the present work. The alloy melting occurred at around 735 °C in a vacuum or with an inert atmosphere at an electric oven (Inductotherm Group, Brazil). After adjusting the alloy chemical composition in the preparation oven, the liquid metal was solidified into cylindrical billets with a diameter of 178 mm and a length of 6 meters at room temperature. The industrially cast billets underwent homogenization, extrusion and solubilization, tempering, and artificial aging treatment processes. An Applied Research Laboratories (ARL) optical emission spectrometer (OES), model 3460 was used to quantify the material chemical elements. The already homogenized billets were preheated for 4 hours at around 460 °C and then cut into 500 mm billets to be hot deformed in the extrusion process, in which the thickness was reduced to 3.2 mm.

The extrusion tool was heated for 4 to 6 hours in a separate oven to enter the process, with an average temperature of 450 to 500 °C. The extruded profiles were cooled using water and air spray to maintain the solubilization. After solubilization, the extruded bars pass to the stretching process with 0.3% strain to improve straightness along the length, and through the cutting process. The samples were taken after the stretching step to carry out tests and aging heat treatments on a laboratory scale.

The billet homogenization was performed in a muffle furnace (Fortelab, Brazil) model ML-1300/40 in two different soaking stages, first at 500 and the second at 550 °C. After both soaking stages, the material was cooled to room temperature in air. The emerging temperature of 520 °C was established for profile solubilization. To define the best parameters for the heat treatment of artificial aging, some preliminary tests were carried out on a laboratory scale in a muffle oven from the brand Metaltrend. The best aging heat treatment was performed by heating the extruded profile for 3 h to 180 ºC, keeping it at that temperature for 8 h so that the precipitation reactions of compounds in the desired quantities and sizes could occur. The artificial aging on an industrial scale was carried out in an OMAV brand gas oven with two temperature control thermocouples and a ventilation system to maintain temperature homogeneity.

The microstructure was characterized by optical microscopy (OM) (Olympus, Confocal OLS-4100, Japan), scanning electron microscopy (SEM) (JEOL, JSM 7100FTLV, USA) and transmission electron microscopy (TEM) (JEOL, JEM-2100, USA) techniques, and the X-ray diffraction technique (XRD) (HIGAKU, Miniflex, Japan) aimed at identifying and quantifying the existing constituents.

The metallographic examination for microstructural characterization involved embedding the sample in bakelite, followed by surface grinding using progressively abrasive papers, advancing to 1200 grit. After grinding, the samples were polished using a 1 µm diamond paste, and a 0.4 µm colloidal silica solution.

Energy Dispersive Spectroscopy (EDS) and Electron Backscatter Diffraction (EBSD) resources were used In the SEM analyses. The EDS analyses were performed to identify and quantify the constituents present in the AlSiMg(Cu) alloy at the end of each stage of the industrial processing. The larger constituents (greater than 500 nm) were examined at the end of each of the 4 stages of the industrial processing and scanning was performed in approximately 2120 sampling fields, with a magnification of 2,000 X. While the smaller ones (less than 500 nm) were only examined in the solubilized and aged samples and a smaller number of fields, in 20, with a magnification of 15,000 X.

EBSD analyses were performed to evaluate the grain size distribution of the Al phase (solidified and homogenized samples), to specify grain boundaries and sub-contours, to evaluate the preferential texture (solubilized and aged samples) and to differentiate and quantify the recrystallized, recovered and hardened regions of the alloy (solubilized and aged samples). The billet samples were examined in an area corresponding to 1.19 x 0.893 mm while the extruded profiles were analyzed throughout the entire thickness.

TEM analyses were performed to record and determine the chemical elements present in the small constituents, with a size of less than 100 nm, existing in the alloy through EDS spot analyses.

XRD analysis was performed to identify and measure the volumetric fraction of the constituents, serving as a basis for comparison with the results of measurements obtained by EDS.

Vickers microhardness (Future-Tech Corp FM-700, Japan) measurements were performed on samples. The tensile tests were carried out at a deformation speed of 7.5 mm/min in the EMIC equipment, model DL 10000, according to the ASTM E8 standard [11].

The tests were carried out on flat specimens of 100 mm in length taken from the solubilized and aged profiles. The stress-strain curves of the profiles were obtained, and the yield strength (YS), the tensile strength limit (TS), and the elastic ratio were measured. The specimens for the tensile tests were obtained from the flat surface of the extruded profile and cut according to the standard ABNT NBR 7549 [12].

3 Results

The 6013-alloy chemical composition with the specification according to the ISO 209 standard is shown in Table 1. A higher content of the main elements (Si and Mg) is observed compared to the most common 6XXX series alloys. The Fe contaminant element is present in a significant percentage, which is not desirable for these alloys due to the formation of intermetallics that act as embrittlers.

To prevent the instantaneous precipitates dissolution in the grain boundaries (which causes billet fragility), homogenization can be performed at a slow rate and two temperature levels. After reaching the second level temperature, soaking is performed again for 4 hours to ensure maximum compound dissolution, solubilization, and redistribution of the solute in the Al matrix. It is important to have good temperature control so that it is not close to the solidus line, with a high risk of melting the α phase, which can therefore be adopted as a limit to carry out the alloy heat treatment with maximum efficiency and safety.

During extrusion, part of the energy was introduced into the material, and the rest was dissipated in heat. The billets were sawn into small ones (500 mm in length) to reduce the shear force of processes in which alloys that are more "loaded" with alloying elements are worked on. As the friction force between the billet and the container wall depends on the contact area between both, a decrease in the billet length provides a considerable reduction in the friction force. Therefore, a more significant portion of the extrusion force can be used to overcome the shear [13].

The 6013-alloy microstructures at the different stages can be seen in Figure 1. As the α phase exhibits a low capacity to retain solutes, and because of the casting process features it owns columnar grain growth from the mold walls, there was a great tendency to reject the solutes towards the solidification front, and consequently, the phases existing in the 6013-alloy were almost entirely precipitated in the α phase grain boundaries.

The second phase volumetric fraction in the as-cast state was 2.22%. After the billet homogenization process, the phases concentrated in the grain boundaries were dissolved, and chemical elements resulting from this dissolution were solubilized in the α phase, reducing the to 2.00%. In

Table 1. The 6013-alloy chemical composition in % mass

Reference	Si	Fe	Cu	Mn	Mg	Cr	Zn	Ti
Standard	0.60-1.00	0.50 max.	0.60-1.10	0.20-0.80	0.80-1.20	0.10 max.	0.25 max.	0.10 max.
Sample	0.91	0.22	0.80	0.27	0.95	0.08	0.003	0.035

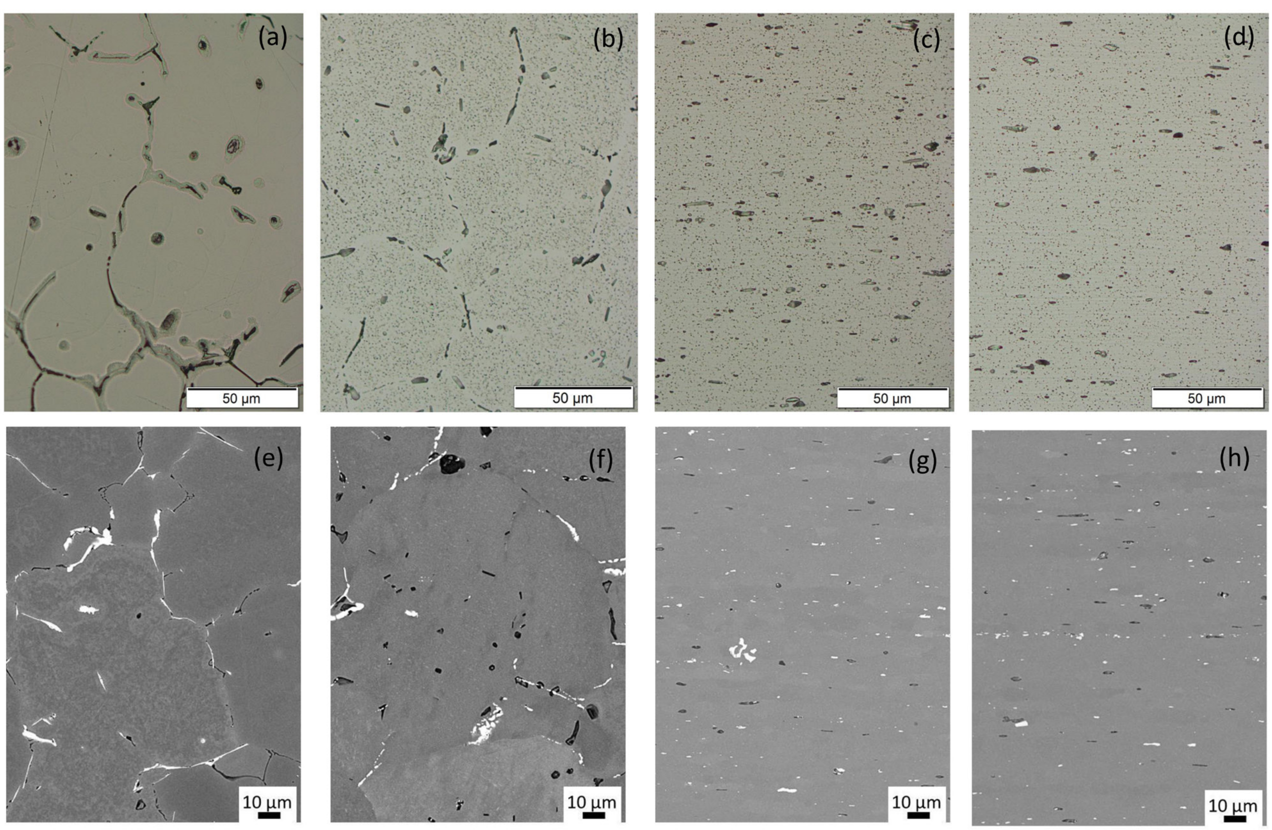

Figure 1. Optical microscopy (a, b, c, d) and SEM using EBSD (e, f, g, h) of the 6013-alloy microstructure of the billet after the completion of solidification steps (a, e), homogenization (b, f) and profile after extrusion/solubilization (c, g) and aging (d, h).

the homogenization step, many chemical elements were solubilized into the Al matrix and, a greater number of phases were precipitated in the matrix during cooling, with precipitates having a smaller size and a more homogeneous distribution in the billet, as shown in Figures 1b and 1f. After the homogenization, the billet was reheated before starting the extrusion. The heat generated by the frictional forces during the extrusion process, increases formability and promotes the redissolution of precipitates, causing the solubilization of alloying elements into the α-phase matrix. Due to this, there was a considerable decrease in the second phase volumetric fraction concerning that verified in the homogenized billet, presenting a measured value of 0.71%. In the microstructure shown in Figures 1d and 1g, the phases exhibited more refined and dispersed in the α matrix, with less precipitation. The solubilized profile was then subjected to the aging heat treatment. Although the images presented in Figures 1d and 1h do not demonstrate significant alterations in the microstructure, the EDS results indicated a marked phase precipitation of 1.55%, more than doubling the volumetric fraction about the solubilized profile. This increase in the number of precipitated phases during aging was mainly due to the Mg_2Si phase precipitation. Figure 2 shows the volume fractions results analyzed using EDS.

The 6013 alloy contains both Mg and Si, which favors the formation of intermetallic compounds, such as Mg_2Si, due to the affinity of these elements to form this compound. This compound is highly stable in these aluminum alloys, because it is thermodynamically favored over others during solidification and the aging process [14]. The predominant phases in 6013-alloy were Mg_2Si, which was already expected, and those made of Fe, including Al_9Fe_2Si and $Al_{16}FeMn_3$. At the billet solidification end, the EDS indicated that the precipitated phases were practically Mg_2Si, $Al_9Fe_2Si_2$, and Al_2Cu. The Si, $Al_{16}FeMn_3$, and Al_3Ti phases precipitated in small amounts compared to the others. An increase in the Mg_2Si phase amount can be observed after homogenization. The Al_2Cu and $Al_9Fe_2Si_2$ phases were partially dissolved, while there was an increase in the $Al_{16}FeMn_3$ phase volumetric fraction.

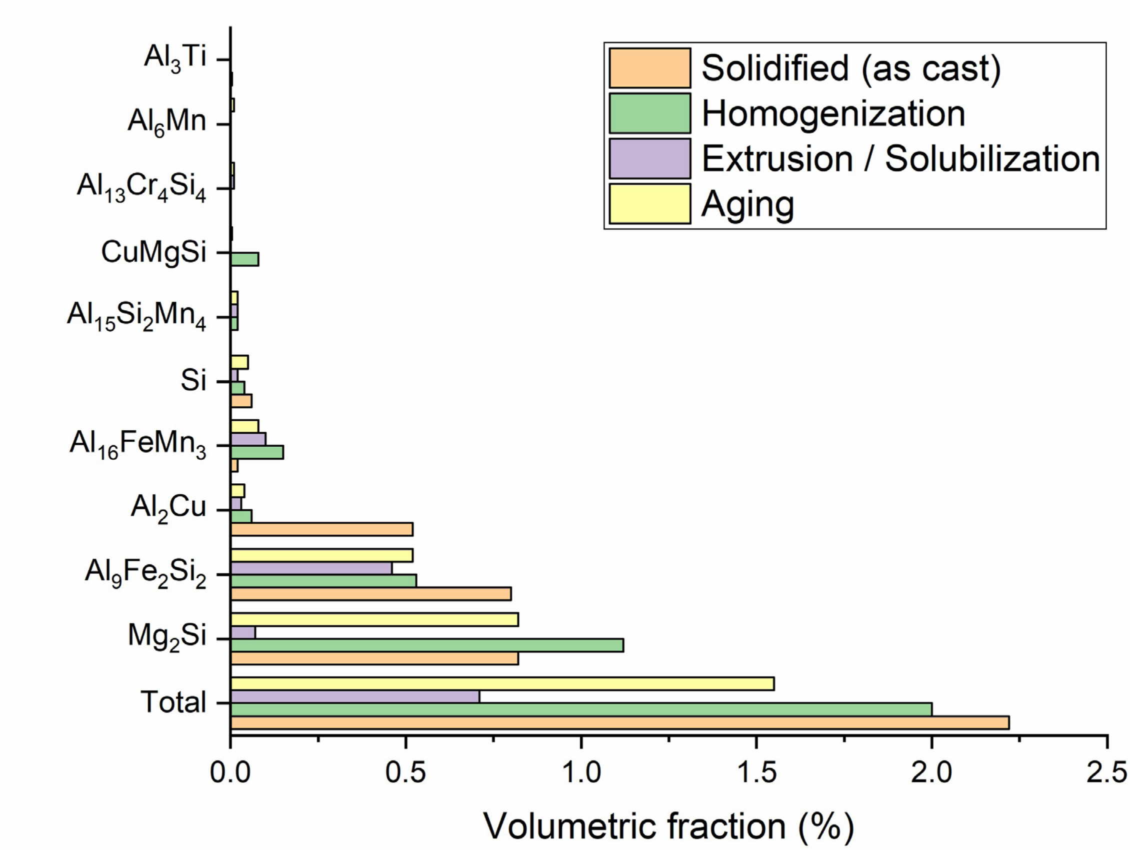

Figure 2. Graph of the precipitated phases volumetric fraction in 6013-alloy along the billet processing steps estimated by EDS: after solidification, homogenization, extrusion and solubilization, and aging.

Homogenization caused the AlCuMgSi phase precipitation, providing kinetic conditions for the reaction occurrence. On the other hand, metallic Si practically did not have its volumetric fraction modified. The phases precipitation was delayed after the extruded and solubilized profile cooling step. In consequence, only the most stable phases, with favored kinetics of the 6013-alloy was found. In the last processing step, aging enhanced the Mg_2Si precipitation. The other phases had only a small change in their amounts concerning the solubilized profile.

The XRD results were very close to those found by EDS and can be seen in Figure 3. It is important to notice that there is a difference between the α-AlFeSi (Al_8Fe_2Si) and β-AlFeSi (Al_5FeSi) phases presented in the XRD results. The β phase is known for its monoclinic or orthorhombic crystalline structure and morphology in the shape of needles or plates. On the other hand, the α phase presents a hexagonal crystalline structure and a more globular morphology [15]. However, both phases are harsh and incoherent with the α matrix. The fact that these hard phases do not accompany the matrix plastic deformation causes cracks to be nucleated at the interphase interface, reducing the ductility and, eventually, the alloy strength limit. Although they contribute to the alloy hardening alloy, their presence is considered, in general, undesirable because it impairs the plastic deformation capacity of aluminum alloys, a characteristic required for possible applications in car body components that require extensive plastic deformation.

The β phase, due to its needle-shaped morphology, exhibits greater potential to harm the mechanical properties of the alloy in relation to the α phase, which has a more globular morphology.

When examining the solidified billet diffractogram, the presence was evident that the β-AlFeSi phase, as shown in Figure 3a. Considering that during solidification there was many chemical elements segregated in the solidification front of the α phase and that the cooling speed of the solidified billet was relatively slow, it is reasonable to consider that the β phase is a more stable condition of the AlFeSi compound in relation to the α phase. The EBSD images of the microstructure shown in Figure 1 show brightly contrasting constituents in the 6013-alloy. Spot EDS analyses indicated the existence of Fe, Mn, and Si in these constituents. Figure 4 shows the presence of these elements in the solidified billet microstructure.

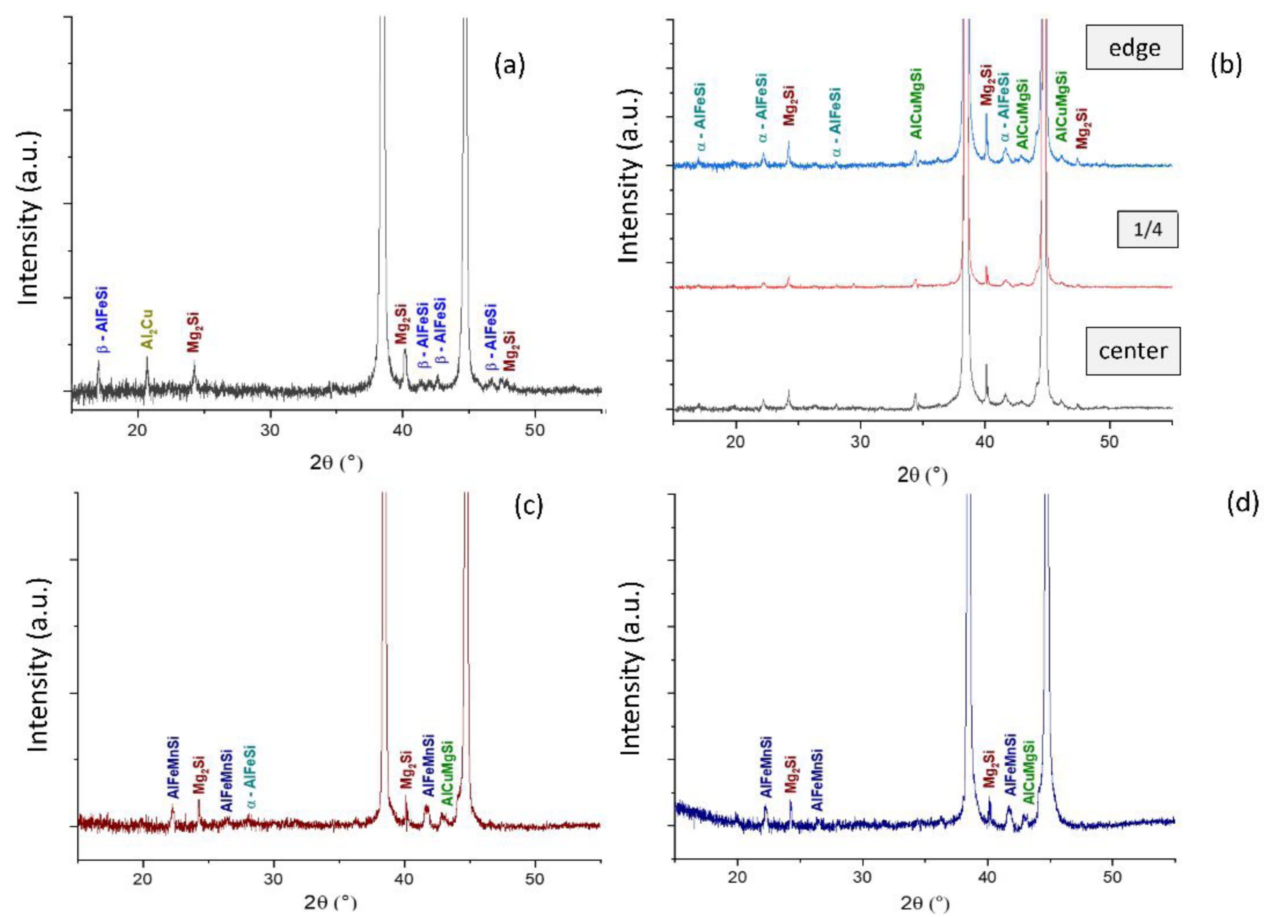

Figure 3. X-ray diffractograms of 6013-alloy at the end of each stage of industrial processing, of the billet after the solidification (a) and homogenization (b) stages, and of the profiles after extrusion and solubilization (c) and after aging (d).

Compared with the diffractogram of the billet after homogenization, the same phases were verified. Compared with the solidified billet, the β-AlFeSi phase was no longer observed and, in its place, precipitation of the α-AlFeSi phase occurred. Homogenization caused the precipitation of the AlCuMgSi phase, which was not observed in the solidified billet. The hypothesis is that, with the billet heating, there was the complete dissolution of Al_2Cu and almost all the Mg_2Si. With a large amount of Mg, Cu, and Si available in α phase, the cooling of the billet may have caused a delay in the Al_2Cu and Mg_2Si phases precipitation, favoring the AlCuMgSi phase precipitation during cooling. Based on the diffractograms presented in Figures 3c and 3d, it can be observed that the billet cooling possibly suppressed the Al_2Cu and Al_3Ti phases formation. And that there was a progressive transition from the α-AlFeSi phase to the AlFeMnSi phase, less harmful to the alloy mechanical properties, as previously reported by Ji et al. [15]. Therefore, it can be concluded that the clear contrast phases in the microstructure of the solubilized and aged profiles correspond, for the most part, to the AlFeMnSi phase, as seen in Figure 1g and 1h. The EDS results regarding the Si phase confirmed the presence of this phase in the alloy in all stages of industrial processing. Therefore, considering adjusting the chemical composition it might be important so that this excess Si is incorporated into the phases that contain Si in their constitution, such as Mg_2Si, enhancing the product mechanical properties. Figure 5 shows the 6013-alloy microstructures with phase identification in color scale, obtained by EDS, aiming to facilitate the phase distribution visualization at the end of each processing step.

In Figure 6 can be seen the solidified and homogenized billets microstructures whose were obtained via EBSD. The high-angle grain boundaries are represented in black, and the low-angle grain boundaries in red in Figures 6b and 6e. In both cases, the microstructures were homogeneous, with grains with an aspect ratio of around 1 and free of work hardening. The grain diameter distribution is shown in Figures 6c and 6f.

The large number of existing grains up to 40 µm was due to considering, in the statistics, the high-angle grain boundaries of the interphase interfaces inside the grains in Figure 6, which justifies the high dispersion when measuring the average diameter. In general, homogenization did not modify the average α-Al phase grain diameter,

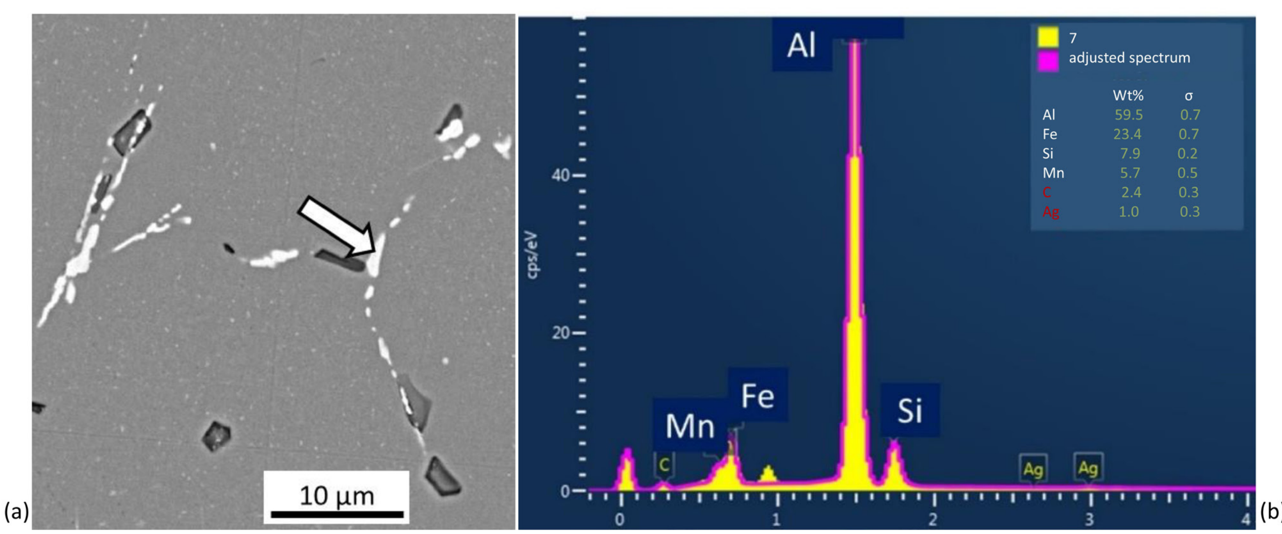

Figure 4. (a) Image by SEM of the 6013-alloy from the solidified billet and (b) EDS spectrum representing the light contrast constituents indicated by the arrow.

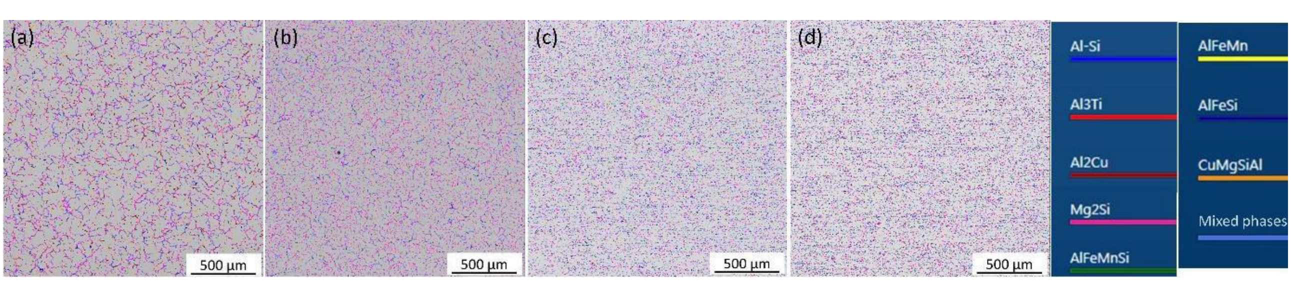

Figure 5. Images obtained by EDS in the SEM of the 6013-alloy microstructure in the conditions: (a) as cast, after (b) homogenization, (c) extrusion / solubilization and (d) aging. Note: The Si phase is identified as Al-Si.

with measurements around 91 μm. However, the number of interfaces created during homogenization, including the low and high-angle ones, was considerably higher due to the change in the precipitation location towards the interior of the α phase, as shown in Figures 6b and 6e.

Although the appearance of the grains showed the same formation pattern between the solubilized and aged profiles, this was quite different from that formed in the billets. The billet was reheated to 460 °C after homogenization so the extrusion could be carried out. The profile was quickly cooled to room temperature after the immersion in the extrusion die at 520 °C. During extrusion, a severe plastic deformation occurred by shear mode near the billet surface, where many slip systems were activated, and this mode was reduced towards the profile thickness center. The profile microstructure resulting from this extrusion process was quite heterogeneous, with a mixture of recrystallized, recovered, and hardened regions, which is characteristic of the process itself, as shown in Figure 7.

Figure 7a shows four distinct regions of the extruded and solubilized profile microstructure. Recrystallized and very refined grains were observed in the subsurface region, up to a depth of around 50 μm from the surface. Adjacent to this region to a depth of approximately 100 μm, the grains are also recrystallized, but slightly larger than those immediately below the surface. Between 100 μm and approximately 800 μm in depth, there is a third region with larger, recrystallized grains with a high aspect ratio.

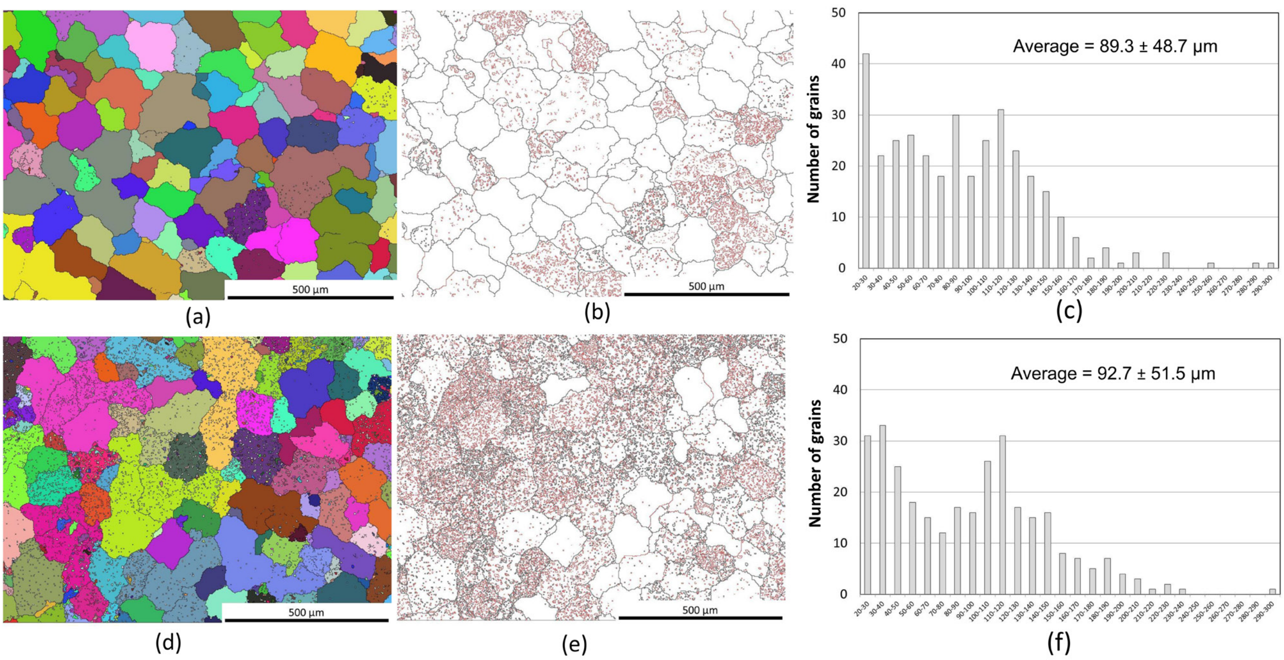

Figure 6. Images obtained by SEM using EBSD of the as cast (a, b) and homogenized (d, e) billet and the distribution of the α-phase grain diameter in 6013-alloy in (c) as cast and (f) homogenized condition.

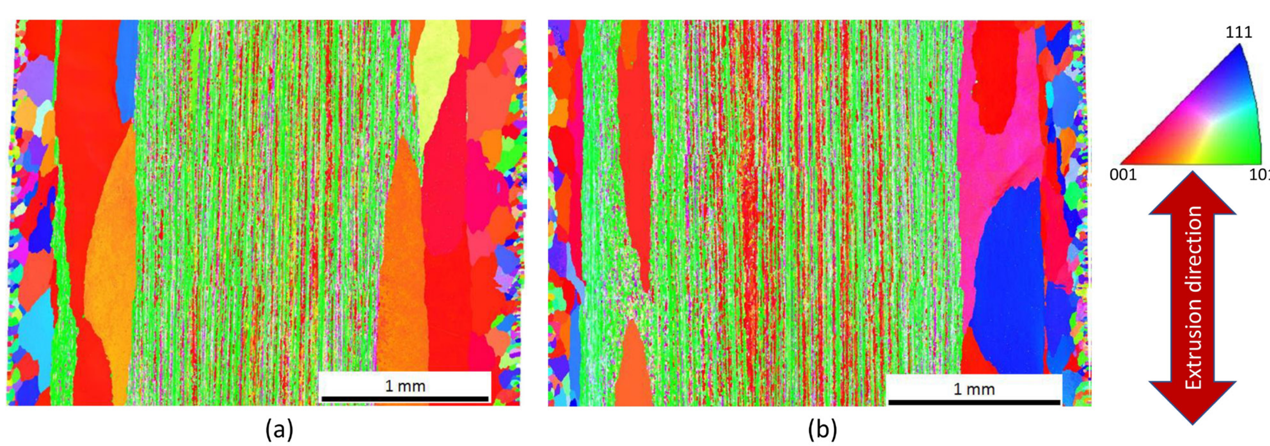

Figure 7. Images obtained on SEM using EBSD with the indication of crystallographic orientation of (a) solubilized profile and (b) aged profile.

There is a mixture of hardened, recovered, and recrystallized grains in the most central region inside the profiles. The grain growth on the surface was possibly limited due to the surface being the first cooling site in the cooling step.

The microstructure appearance in the profiles thickness center indicated many elongated grains in the billet extrusion direction. The quantification results of recrystallized grains indicated that about 85% of the microstructure in this region still consists of hardened grains and only a small fraction of grains (around 9%) consisted of recrystallized grains. The results of this quantification are shown in Figure 8. The short time after the extrusion that the profile remained at high temperatures until cooling could explain why that recrystallization was not completed in the entire solubilized profile. Furthermore, the solubilized profile reheating at 180 °C for 8 h did not change the α phase grains morphology, keeping hardened, recovered, and recrystallized grain fractions unchanged.

The mechanical properties in terms of tension and hardness of the solubilized and aged 6013- alloy profiles are presented in Table 2. In general, the mechanical properties results showed low dispersion. The elastic ratio remained at around 0.56, indicating that the solubilized profile exhibits good strain-hardening capacity. After aging, there was a pronounced increase in the profile mechanical strength, both the yield strength (YS) and the tensile strength (TS) were increased. The elastic ratio was around 0.90, indicating a less strain-hardening capacity compared to the solubilized profile. As expected, the hardness values (HV) are consistent with the tensile tests results.

The size particle distribution after aging, and after extrusion and solubilization is shown in Figure 9. Examining the size distribution of phases smaller than 30 nm, in a sampling of 150 particles identified in the TEM, it was found that the profile after the aging heat treatment showed a greater number of phases with a size smaller than 6 nm, as shown in Figure 9a. In the solubilized profile, phases smaller than 6 nm were precipitated in smaller amounts, as shown in Figure 9b.

EDS analyses carried out on the smaller precipitates indicated the existence of Al, Cu, Mg, and Si, indicating the occurrence of precipitation of compounds such as Al_2Cu, Mg_2Si, and the compound $Al_3Cu_2Mg_9Si_7$, that is known as the Q-phase in the solubilized profile, as shown in Figures 10a and 10b. The Q-phase forms a thermodynamically stable precipitate formed during aging in the quaternary Al-Cu-Mg-Si system and has been widely used for strengthening in an Al matrix [16]. After aging, these same elements were identified in clusters of precipitates along low-angle grain boundaries and disagreements, as shown in Figure 10c and 10d. This precipitation occurred on a larger scale in the aging process and can be proven through the results of the measurement of the volumetric fraction of the constituents, which indicated an increase in the volumetric fraction of Mg_2Si and Al_2Cu. When examining the tensile specimens fracture surface removed from the aged profile, it was possible to observe many phases containing Fe associated with the shear microcavities, shown in Figure 11.

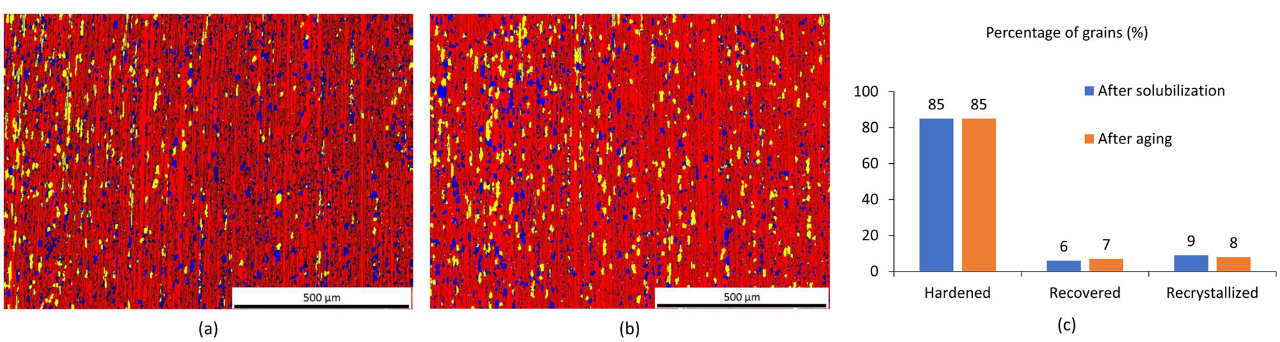

Figure 8. Images obtained by SEM using EBSD at the thickness center of the profiles, indicating the hardened (red), recovered (yellow), and recrystallized (blue) regions of the extruded and solubilized profile (a) and the aged profile (b). And (c) the fraction of hardened, recovered, and recrystallized grains in the solubilized and aged profiles.

Table 2. Tensile mechanical properties and hardness of the solubilized and the aged profile of 6013 alloy

Specimen	Condition	YS (MPa)	TS (MPa)	YS/TS	HV
1	Solubilized	184	335	0.55	
2		194	337	0.58	
3		187	332	0.56	
Average		188 ± 4	335 ± 3	0.56	89 ± 2
1	Aged	353	391	0.90	
2		351	389	0.90	
3		353	390	0.91	
Average		352 ± 1	390 ± 1	0.90	118 ± 1

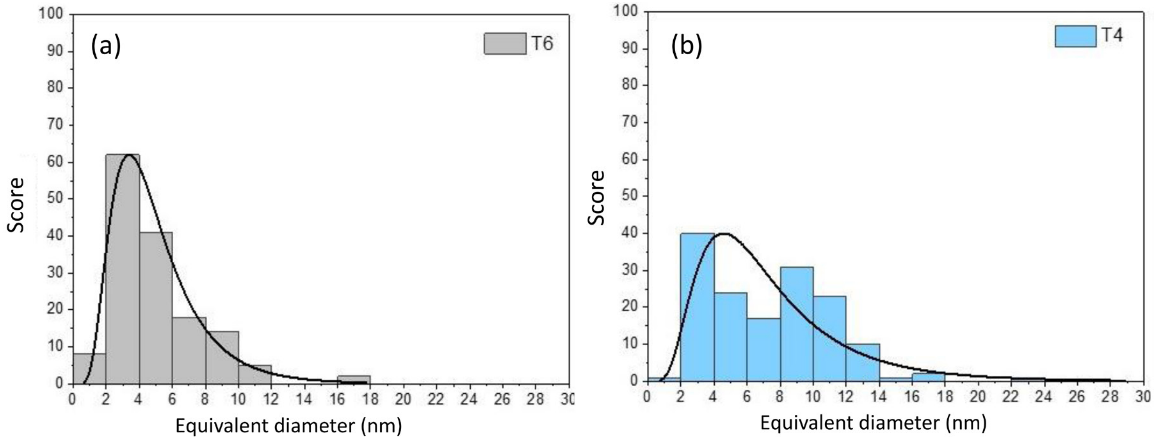

Figure 9. The size particle distribution smaller than 30 nm in profiles (a) after aging and (b) after extrusion and solubilization.

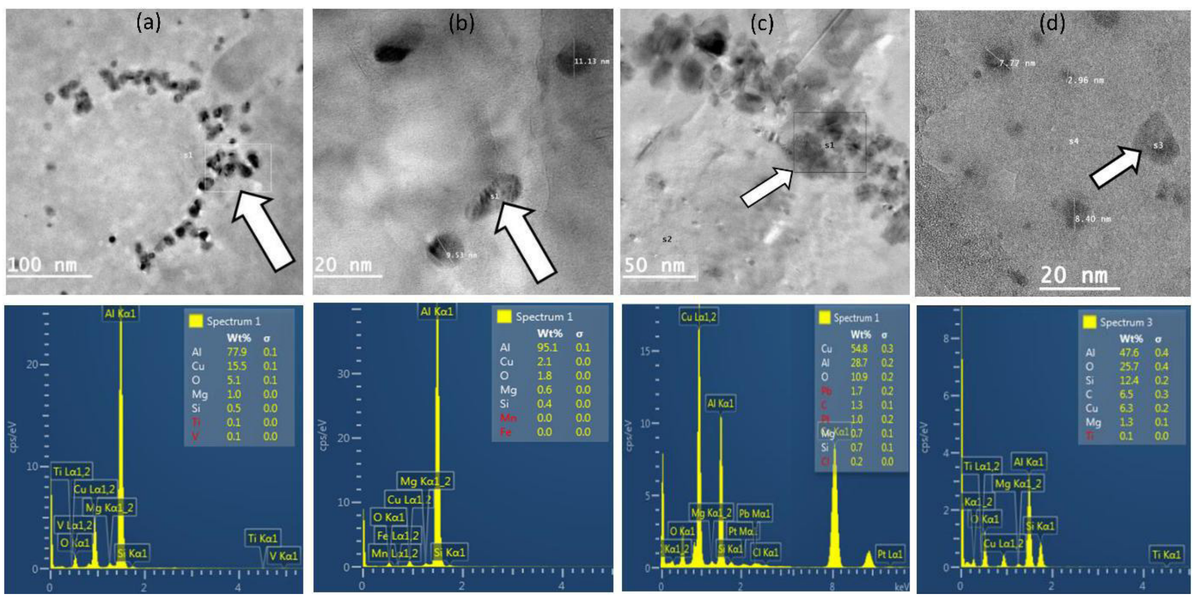

Figure 10. TEM images of precipitates with Al, Cu, Mg, and Si content with respective EDS spectra, in the solubilized profile (a) agglomerated phases and (b) selected precipitate and in the aged profile, (c) agglomerated phases and (d) selected precipitate (regions identified by arrows).

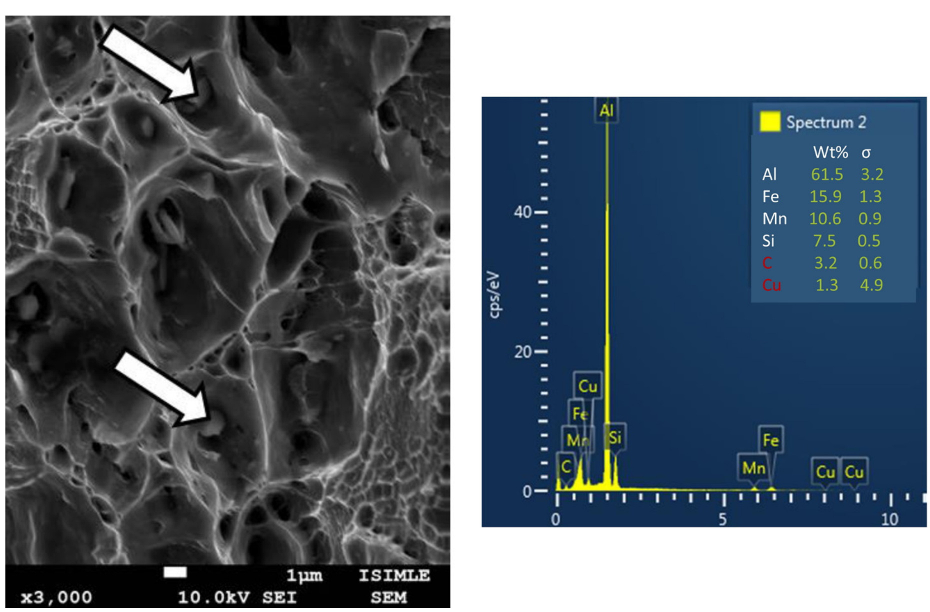

Figure 11. SEM image of (a) the fracture surface of an aged profile tensile specimen with respective EDS spectra (b) indicating the presence of elements Al, Fe, Mn, and Si in the precipitates identified in the existing shear microcavities (regions indicated by arrows).

4 Conclusions

The microstructural characterization and tensile mechanical properties of 6013 aluminum alloy at various stages of industrial processing reveal the following: At the end of solidification, the material exhibits a coarse microstructure with precipitated phases primarily at the grain boundaries, comprising 2.2% of the total volumetric fraction, including Mg_2Si, β-AlFeSi, Al_2Cu, and Si. After the homogenization heat treatment, the α phase morphology remains unchanged, but the distribution of the phases and volumetric fraction are altered, yielding α-AlFeSi, Q-phase, Mg_2Si, Al_2Cu, and Si more homogeneously distributed and reducing their grain boundary fractions, with a total second phase volumetric fraction of 2.0%.

Following extrusion and solubilization, the α phase is heterogeneously distributed with recrystallized grains near the surface and hardened grains inside, featuring finely dispersed AlFeMnSi, Mg_2Si, Q-phase, Al_2Cu, and Si, reducing the second phase volumetric fraction to 0.71%. Aging heat treatment does not change the α phase morphology but significantly increases the size of the phases and volumetric fraction to 1.55%, with an increase in Mg_2Si, the main hardener. Consequently, the aging heat treatment markedly enhances the mechanical strength of the extruded profile.

References

1 Sharma AK, Bhandari R, Aherwar A, Rimašauskiene R, Pinca-Bretotean C. A study of advancement in application opportunities of aluminum metal matrix composites. Materials Today: Proceedings. 2020;26:2419-2424.

2 Ivanoff TA, Carter JT, Hector LG, Taleff EM. Retrogression and reaging applied to warm forming of high-strength aluminum alloy AA7075-T6 sheet. Metallurgical and Materials Transactions. A, Physical Metallurgy and Materials Science. 2019;50(3):1545-1561.

3 Hu J, Zhang W, Fu D, Teng J, Zhang H. Improvement of the mechanical properties of Al–Mg–Si alloys with nano-scale precipitates after repetitive continuous extrusion forming and T8 tempering. Journal of Materials Research and Technology. 2019;8(6):5950-5960.

4 Tomstad AJ, Thomesen S, Børvik T, Hopperstad OS. Effects of constituent particle content on ductile fracture in isotropic and anisotropic 6000-series aluminium alloys. Materials Science and Engineering A. 2021;820:141420.

5 Tomstad AJ, Frodal BH, Børvik T, Hopperstad OS. Influence of particle content on the ductility of extruded non-recrystallized aluminium alloys subjected to shear loading. Materials Science and Engineering A. 2022;850:143409.

6 Thomesen S, Hopperstad OS, Myhr OR, Børvik T. Influence of stress state on plastic flow and ductile fracture of three 6000-series aluminium alloys. Materials Science and Engineering A. 2020;783:139295.

7 Lei G, Wang B, Lu J, Wang C, Li Y, Luo F. Microstructure, mechanical properties, and corrosion resistance of continuous heating aging 6013 aluminum alloy. Journal of Materials Research and Technology. 2022;18:370-383.

8 Bakare F. Effect of extrusion processing on the microstructure and mechanical properties of AA6082 aluminium alloys [thesis]. Sydney: Macquarie University; 2019.

9 Odoh D. Effect of alloy composition on the hot deformation behavior, extrudability and mechanical properties of AA6XXX aluminum alloys [thesis]. Waterloo: University of Waterloo; 2017 [cited 2025 Jan 13]. Available at: http://hdl.handle.net/10012/12116

10 Bai X, Kustas A, Chandrasekar S, Trumble K. Large strain extrusion machining on 6013 aluminum alloy. In: Williams E, editor. Light metals 2016. Hoboken: John Wiley & Sons; 2016. p. 225-229.

11 American Society for Testing and Materials – ASTM. ASTM E8/E8M-11: standard test methods for tension testing of metallic materials. West Conshohocken: ASTM; 2011.

12 Associação Brasileira de Normas Técnicas – ABNT. ABNT NBR 7549: alumínio e suas ligas: produtos laminados, extrudados, fundidos, forjados e sinterizados: ensaio de tração. Rio de Janeiro: ABNT; 2021.

13 Hattori CS, Almeida GFC, Gonçalves RLP, Santos RG, Souza RC, Silva WC, et al. Microstructure and fatigue properties of extruded aluminum alloys 7046 and 7108 for automotive applications. Journal of Materials Research and Technology. 2021;14:2970-2981.

14 Ji Y, Zhong H, Hu P, Guo F. Use of thermodynamic calculation to predict the effect of Si on the ageing behavior of Al–Mg–Si–Cu alloys. Materials & Design. 2011;32(5):2974-2977.

15 Ji S, Yang W, Gao F, Watson D, Fan Z. Effect of iron on the microstructure and mechanical property of AlMgSiMn and AlMgSi diecast alloys. Materials Science and Engineering A. 2013;564:130-139.

16 Kim K, Bobel A, Brajuskovic V, Zhou BC, Walker M, Olson GB, et al. Energetics of native defects, solute partitioning, and interfacial energy of Q precipitate in Al-Cu-Mg-Si alloys. Acta Materialia. 2018;154:207-219.

Received: 15 July 2024
Accepted: 30 Mar. 2025

Editor-in-charge: Paula Fernanda da Silva Farina